Vortex dynamics resulting from the interaction between two NACA 23 012 airfoils

Thierry M. Faure, Laurent Hétru, Olivier Montagnier

50h 3AF International Conference
on Applied Aerodynamics
29-30 March – 01 April 2015, Toulouse - France

FP10-2015-faure

Vortex dynamics resulting from the interaction between two NACA 23 012 airfoils

Thierry M. Faure [1,2], Laurent Hétru [1], Olivier Montagnier [1,3]

[1] Centre de Recherche de l'Armée de l'air, École de l'Air, B.A. 701, 13661 Salon-de-Provence, France,
Email: thierry.faure@defense.gouv.fr, laurent.hetru@defense.gouv.fr, olivier.montagnier@defense.gouv.fr
[2] Laboratoire d'Informatique pour la Mécanique et les Sciences de l'Ingénieur, bâtiment 508,
rue J. Von Neumann 91403 Orsay, France
[3] Laboratoire de Mécanique et d'Acoustique, 31 chemin Joseph Aiguier, 13402 Marseille, France

ABSTRACT

An experimental study of the interaction between two airfoils, corresponding to a T-tail aircraft configuration, is implemented in a wind tunnel for a range of medium Reynolds numbers. Measurement of aerodynamic forces is carried out by strain gauges and the velocity field is obtained by particle image velocimetry. The study focuses on large angles-of-attack configurations, corresponding to detached flows on the airfoils and the presence of a downstream vortex shedding. Phase averages of the velocity fields are made building the flow time development. A lift modulation depending on geometric parameters and resulting from different pathlines of the shedding vortices, is discussed.

1. INTRODUCTION

Aerodynamics of airfoils operated on moderate Reynolds numbers, in the range 10^4 to 10^5, has recently gained in importance, with a variety of applications, such as micro air vehicles (MAV), unmanned air vehicles (UAV) and low speed high-altitude long endurance aircraft (HALE) [1]. Many studies are focusing on rotor aircrafts but there is a lack of publication on classical wing-tail configuration for that Reynolds number range. In order to get the aerodynamic coupling between the vortices generated by the detached flow from an upstream airfoil (wing) on a downstream airfoil (tail), a two-dimensional reference experiment is used for velocity characterization. The aim is to understand the flow properties resulting from the wakes interaction and the influence of the detached flow region with the parameters (angle-of-attack, setting angle of the tail …) but also to catch the dynamics of vortices, created for large values of angle-of-attack, by the development of Von Kármán instability. A possible application of that study is the understanding of deep stall phenomenon, typical of large angles-of-attack for T-tail aircraft configurations, where the tail is in the detached flow of the wing [2]. That attitude corresponds to a stable equilibrium point, where the tail command is almost ineffective leading to no simple airplane recovering procedure. Velocity measurements are conducted with particle image velocimetry (PIV) and the aerodynamic coefficients on each airfoil are obtained by strain gauges balances. There is a double objective in that study. First, the averaged velocity field is investigated in order to characterize the detached and attached flow regions, the wakes and turbulence levels as function of the angle-of-attack α. These flow features are analyzed in relation with the aerodynamic coefficients. Secondly, a phase-averaging of PIV measurements is carried out in order to build the time development of periodic flow dynamics such as vortex shedding. To do so, from not time-resolved PIV data, it would be necessary to synchronize time-resolved airfoil force signals with PIV fields, and to perform singular value decomposition for reorder the phases. However, the present analysis uses a different approach with direct phase identification from a given position of a vortex [3].

2. EXPERIMENTAL SETUP AND APPARATUS

The experimental setup is made of two NACA 23 012 airfoils in the test section of a closed-loop wind tunnel (Figure 1), with a squared section 45 cm×45 cm. Hereafter, the upstream airfoil will be referred as the wing, and the downstream airfoil as the tail. The flow maximum velocity is 30 m·s^{-1}. The velocity inside the test section is homogeneous with deviations lower than 1% and a residual turbulence lower than 0.3%. The cord of the wing airfoil c is the double of the tail airfoil chord, both of them get a span equals to the test section width. Each airfoil is supported on a single axis fixed in a rotating disk in one wall of the wind tunnel, permitting the angle-of-attack setting and allowing a free optical access from the other side of the wind tunnel. The main drawbacks of this setup are high aspect ratios, of 9 for the wing and 18 for the tail. Although the wing and tail are made of carbon fibers to shift low frequencies, these aspect ratios may result in buffeting for high velocities, limiting the upstream flow velocity to 17.5 m·s^{-1}.

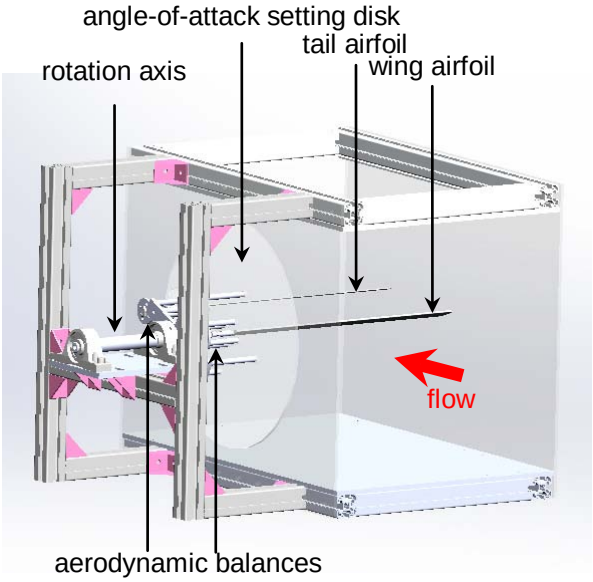

Figure 1. Test section and experimental setup.

The distance between the airfoils can be changed along two perpendicular directions (Figure 2). In the present study, distances between the airfoils leading edges, in the upstream airfoil frame of reference (x_a, z_a) is $\ell_x = 3.19\,c$ and $\ell_z = c$. The global angle-of-attack setting can be fixed by the rotating disk. In addition, the tail airfoil can be adjusted from the wing with a setting angle i_T. An issue on any experimental setup is the blockage by the wind tunnel walls, defined as:

$$B = \frac{S_1 \cup S_2}{S} \qquad (1)$$

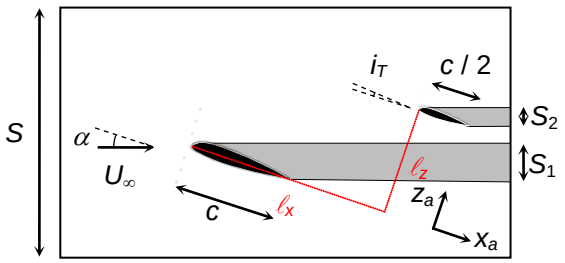

Figure 2. Airfoil configuration and flow blockage.

In the present configuration, to limit the blockage for high angles-of-attack, a chord $c = 50$ mm is chosen for the wing, leading to an angle-of-attack of 30° with a blockage ratio lower than 6% (Figure 3) below which there is no flow distortion [4]. In addition, to avoid any ground effect between the wind tunnel floor or ceiling and the airfoils, these latter are placed in the center of the test section.

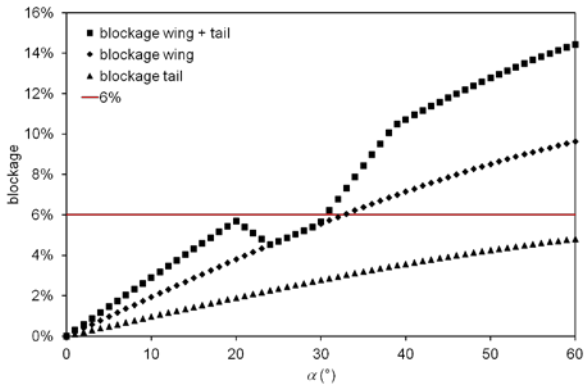

Figure 3. Blockage of the two-airfoil configuration versus angle-of-attack for $i_T = 0°$ (the airfoil thickness is neglected).

The Reynolds number, built on the upstream flow velocity U_∞ and the wing airfoil chord c equals 58 300. The similarity between the experiment and MAV, UAV and HALE applications is generally respected, but not between the experiment and traditional aircrafts. However, as we are mainly interested in detached flows for high angles-of-attack, that condition is not essential. In fact, as it is shown in Figure 4 for a NACA 0012 airfoil, there is no Reynolds number effect on the lift coefficient versus angle-of-attack plot for $\alpha < 5°$ (attached flow region) and $\alpha > 30°$ [5]. PIV frames are recorded with a 12-bit camera with a resolution 2360×1776 pixels. PIV recording frequency is 15 Hz. A Nd:YAG laser is emitting a wavelength 532 nm to generate a light sheet of 0.5 mm in thickness with 200 mJ by pulse. Velocity fields are

obtained with an interrogation window of 32×32 pixels and an overlap of 75%. Averaged velocity and standard deviation of fluctuations are obtained from 500 fields to get relative uncertainties lower than 1%. In order to get a maximum view of the flow, the camera framing is realized in order to get a complete view of the airfoil suction side.

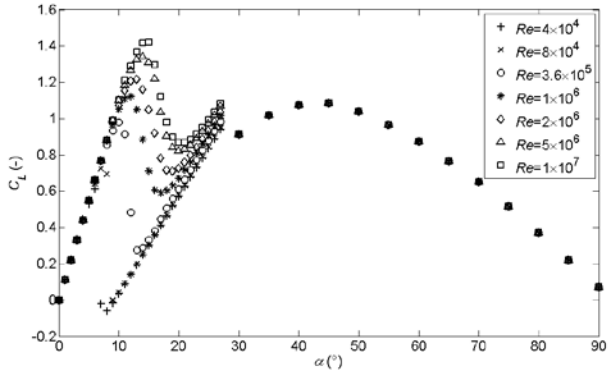

Figure 4. Lift coefficient for a NACA 0012 airfoil versus angle-of-attack for different Reynolds numbers [5].

3. LIFT AND DRAG COEFFICIENTS

A complete database of lift and drag coefficients is obtained for the NACA 23 012 airfoil and angles-of-attack between -20° and 45°, including values beyond the airfoil stall (Figure 5). Such aerodynamic coefficients are available in literature but are limited to angles-of-attack lower than 20°. These data are obtained both for a single airfoil in the test section (Figure 5) but also for the configuration corresponding to a wing-tail interaction (Figure 6). For a single airfoil, the lift and drag coefficients show the same behavior for the wing and for the tail, but the stall point is different and corresponds to $\alpha = 7°$ for the wing and $\alpha = 4°$ for the tail (Figure 5). This difference may be due to an effect of the Reynolds number corresponding to 58 300 for the wing (chord c) and to 29 150 for the tail (chord c / 2). After a minimum, lift coefficient is increasing again after an angle-of-attack around $\alpha = 10°$ and a similar development is found for both airfoils. Note also the decrease of the wing lift coefficient for $\alpha > 33°$, in comparison with the tail lift coefficient, which may be caused by blockage (Figure 3). The data for a single airfoil are in agreement with published lift coefficients for a similar Reynolds number [6]. Drag coefficients are very similar with very low values in the attached flow region. For wing and tail airfoil in interaction with $\ell_x = 3.19\,c$ and $\ell_z = c$, wing lift and drag coefficients are not changed in comparison with the single wing configuration, proving there is no forward potential effect caused by the tail (Figure 6). For the tail airfoil, lift coefficient is similar for negative values of angle-of-attack, but for positive values no stall drop is observed. This may be caused by the wing-tail interaction and the flow forcing, in the tail suction side, resulting from the Von Kármán vortices generated by the wing detached flow. As a consequence, the lift coefficient is increased.

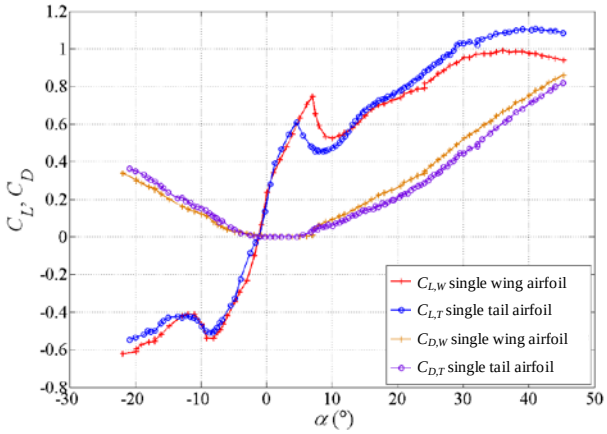

Figure 5. Lift and drag coefficients for a single wing or tail NACA 23 012 airfoil.

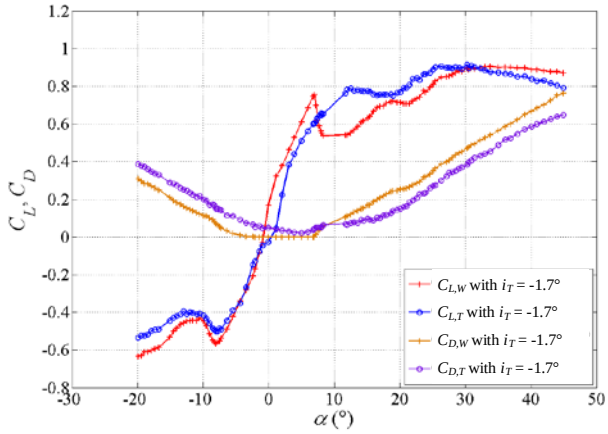

Figure 6. Lift and drag coefficients for wing-tail interaction with $\ell_x = 3.19\,c$ and $\ell_z = c$.

4. FLOW ANALYSIS

Regions masked by the airfoils or affected by light reflections are rejected from the frames before PIV calculation and are represented in white in velocity fields. For an angle-of-attack equal to zero (Figure 7), the flow is attached on the suction side showing a larger velocity. The wakes of both airfoils are identified by velocity deficit and there is no interaction between them. Standard-deviation of axial velocity fluctuations presents slightly positive levels only in the wakes of each airfoil (Figure 8).

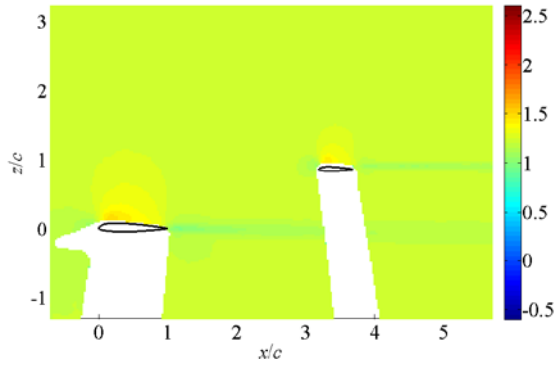

Figure 7. Relative averaged axial velocity for $\alpha = 0°$.

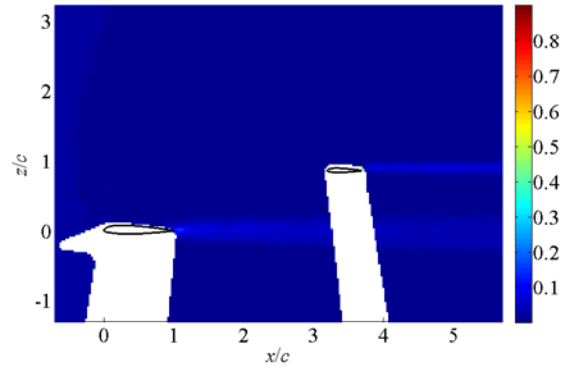

Figure 8. Relative standard deviation of axial velocity fluctuations for $\alpha = 0°$.

For $\alpha = 15°$ the wing and tail suction sides are completely detached, as it is shown by the very low mean axial velocity (Figure 9). The tail is in the wing wake, but beyond the recirculation. The increase in standard deviation of axial velocity fluctuations (Figure 10) observed in the wing suction side is bounded by the shear layer developing around the recirculation. In comparison with $\alpha = 0°$, its maximum value is multiplied by 10. That turbulent wake is the upstream flow for the tail leading to different aerodynamic coefficient in comparison with a single airfoil.

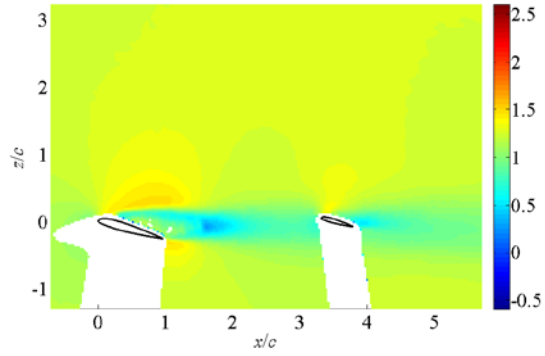

Figure 9. Relative averaged axial velocity for $\alpha = 15°$.

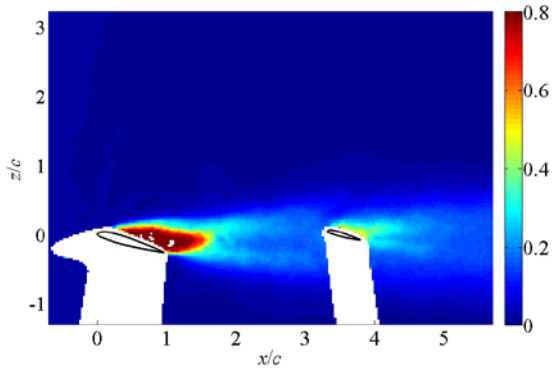

Figure 10. Relative standard deviation of axial velocity fluctuations for $\alpha = 15°$.

For $\alpha = 30°$, the detached flow region is larger, but the tail is not in the recirculation (Figure 11). Standard deviation of axial velocity fluctuations shows a larger region with lower levels in comparison with $\alpha = 15°$ (Figure 12). Note that the lower part of the wing wake turbulent region is enhancing the tail detached suction side flow turbulence level, resulting in larger vertical development of that wake. That result is the evidence of the interaction between the wing wake and the tail detached flow.

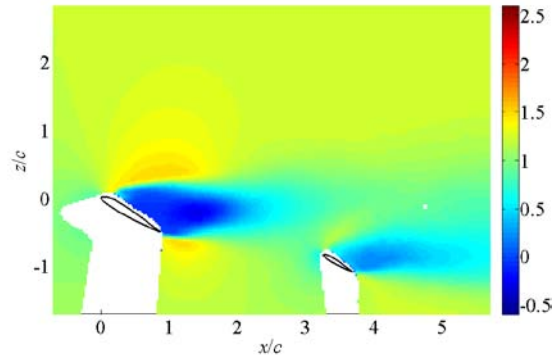

Figure 11. Relative averaged axial velocity for $\alpha = 30°$.

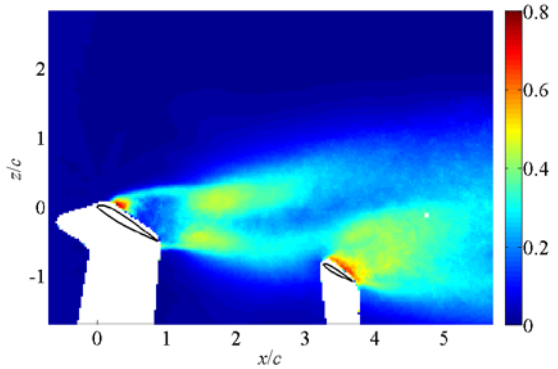

Figure 12. Relative standard deviation of axial velocity fluctuations for $\alpha = 30°$.

The analysis of the instantaneous fields shows the periodic shedding of leading edge vortices (LEVs) and trailing edge vortices (TEVs) of both airfoils, as predicted in numerical simulations [7]. These fields have to be correlated with the time development of aerodynamic forces on each airfoil. For the flow development around an airfoil in vertical motion [8], the LEVs are associated with flow instability of Kelvin-Helmholtz type and the TEVs are associated with the generation of circulation by Kelvin's theorem. In present experiment with a steady flow, we can understand the unsteady periodic LEV shedding as resulting from the unsteady detached flow region on the wing suction side, leading to a global flow distortion and a local change in velocity near the trailing edge, with a TEV shedding.

5. PHASE-AVERAGING

Phase-averaging of velocity fields is addressed with the identification of a vortex position. That analysis can be performed with time-resolved velocity fields [9] or with not time-resolved fields synchronized with a one-point time-resolved signal [10]. In the present study, an alternative method requiring no synchronized measurement with a time-resolved signal is adopted [3]. A reference position along the relative axial position *x/c* is chosen, corresponding to the full development of a detached vortex, with an averaging spatial distance δx. The vortices whose centers are located in the interval $[(x-\delta x)/c, (x+\delta x)/c]$ are considered inside the same class and are averaged. Vortices are characterized on PIV fields with the Γ_2 criterion which is a normalized kinetic moment defined as [11]:

$$\Gamma_2(\vec{x}) = \frac{1}{A} \int_{\vec{x}' \in A} \frac{(\vec{x}' - \vec{x}) \wedge \left[\vec{U}(\vec{x}') - \vec{U}(\vec{x})\right]}{\left\|\vec{x}' - \vec{x}\right\| \left\|\vec{U}(\vec{x}') - \vec{U}(\vec{x})\right\|} d\vec{x}' \qquad (2)$$

with $\vec{x}$ the position in the PIV field and *A* the integration area around that point. The denominator in that relation is very small if the streamlines have a small curvature radius, thus Γ_2 is noise sensitive in irrotational flow regions. In order to suppress that noise, Γ_2 is modified to zero in regions with vorticity below 0.4 s^{-1}. In the present experiment, the noise level is lower in comparison with previous literature [8] which considers a threshold of 4 s^{-1}. Then the Γ_2 values are smoothed inside a circle corresponding to two PIV interrogation windows. A search of a closed contour of levels greater than $2/\pi$ is done in order to validated the presence of a vortex. Γ_2 fields development are decomposed into successive phases ϕ permitting to build a time *t* in relation with the vortex shedding period *T*:

$$t = \left(n + \frac{\phi}{2\pi}\right) T \quad \text{with } n \text{ integer} \qquad (3)$$

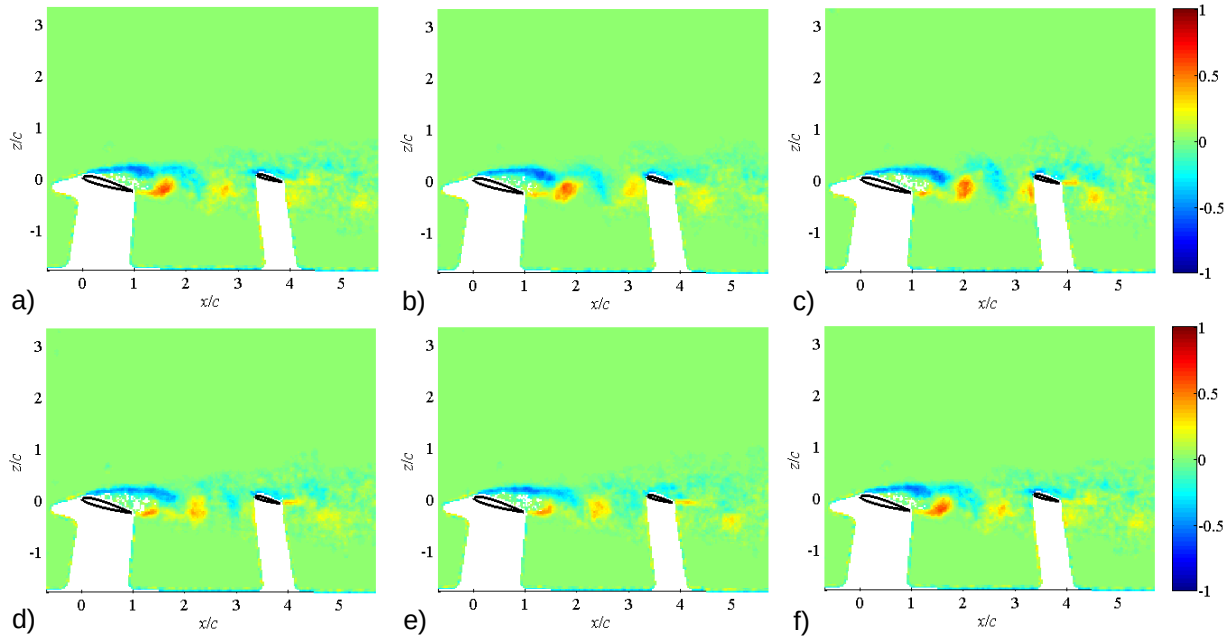

Figure 13. Phase-averaged fields of the Γ_2 criterion for α = 15°, ℓ_x = 3.19 c and ℓ_z = c: a) ϕ = 0°, b) ϕ = 72°, c) ϕ = 144°, d) ϕ = 216°, e) ϕ = 288°, f) ϕ = 360°.

That kind of decomposition is valid with only one reference period, associated with the LEV shedding frequency of the wing airfoil. With a phase interval equal to 18° and an angle-of –attack of 15°, the time-development of LEV and TEV shedding from the wing is built in Figure 13. For $\phi = 72°$ near $x / c = 2$, a LEV is ejected from the suction side recirculation shear layer of the wing (Figure 13-b). That vortex is the result of the development of Kelvin-Helmholtz instability. It is then advected downstream while a TEV is shed at $\phi = 288°$ (Figure 13-e). These vortices shedding alternatively from the leading and trailing edges are in interaction with the tail airfoil pressure side. The pathlines of the wing TEV centers are passing near the tail airfoil pressure side while the wing LEV are impacting the tail leading edge and merge with the tail LEV (Figure 15). The tail TEV pathlines are also identified in the figure; they are above the wing TEV pathlines. That interaction between vortices and the airfoil is a flow forcing of the tail suction side detached flow by the wing LEV. The mechanism associated with periodic LEV shedding yields to a local depression on the tail suction side for the LEV transit times in the tail vicinity. As a result, these times are marked by an increase of tail lift and a decrease of the tail drag. The average of these quantities changes from $C_{L,T} = 0.67$ (Figure 5) for a single tail to $C_{L,T} = 0.75$ (Figure 6) if there is an upstream wing and shedding vortices. Similarly for the drag coefficient, the decrease is from $C_{L,D} = 0.14$ (Figure 5) for a single tail to $C_{L,D} = 0.1$ (Figure 6) for two airfoils in interaction. That lift rise and drag drop cannot be due to a potential effect between the two airfoils, since it is not observed for very low values of angles of attack. As a consequence, the interaction between the tail airfoil and the vortices can be regarded as a control of the tail suction side detached flow by the vortices shedding from the wing and an improvement of the aerodynamic coefficients.

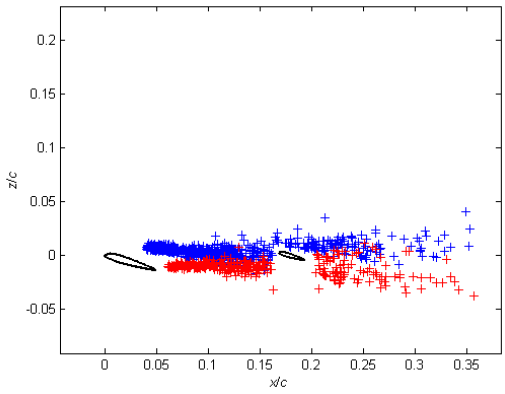

Figure 14. Pathlines of the LEV (blue) and TEV (red) of both airfoils for $\alpha = 15°$.

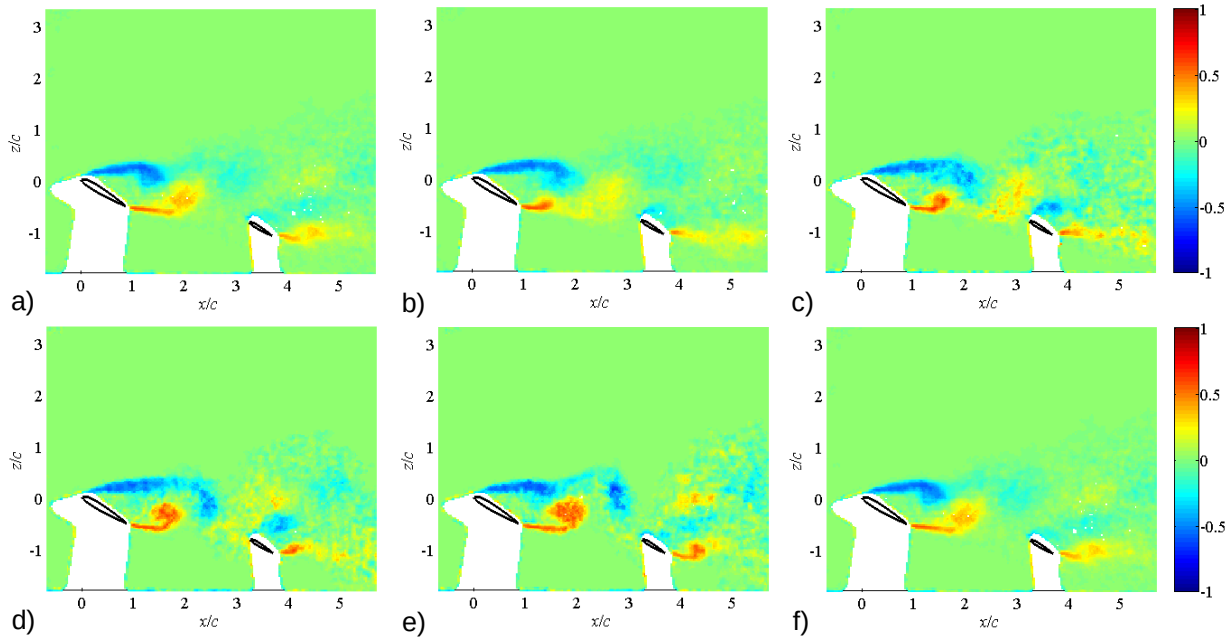

Figure 15. Phase-averaged fields of the Γ_2 criterion for $\alpha = 30°$, $\ell_x = 3.19\ c$ and $\ell_z = c$: a) $\phi = 0°$, b) $\phi = 72°$, c) $\phi = 144°$, d) $\phi = 216°$, e) $\phi = 288°$, f) $\phi = 360°$.

For an angle of attack $\alpha = 30°$, the Γ_2 criterion fields are given for phases $\phi = 0°$, 72°, 144°, 216°, 288°, 360° (Figure 15). The tail airfoil is not completely immersed in the wing airfoil wake, and

we note that the interaction results in a drop of the tail lift coefficient. For phase $\phi = 0°$, the tail LEV is growing in the shear layer formed between the suction side recirculation and a TEV is developed but still connected with the trailing edge (Figure 15-a). This TEV is ejected at $\phi = 72°$ (Figure 15-b) and then advected in the flow, and forces the tail suction side boundary layer. The wing airfoil LEV is ejected with a 180° phase shift (Figure 15-e). Contrary to the case $\alpha = 15°$, there is no merging between the wing LEV and the tail vortices (Figure 16). This leads to a drop of the tail averaged lift coefficient from 0.95 for a single tail to 0.78 for the wing-tail configuration.

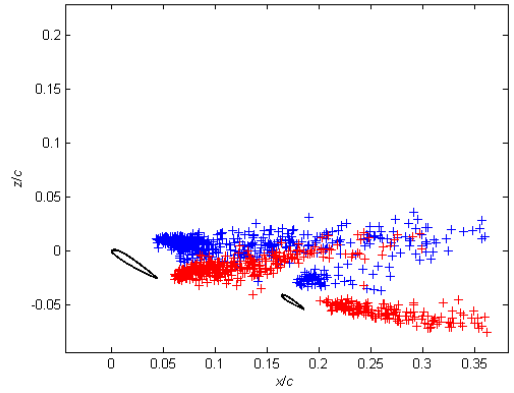

Figure 16. Pathlines of the LEV (blue) and TEV (red) of both airfoils for $\alpha = 30°$.

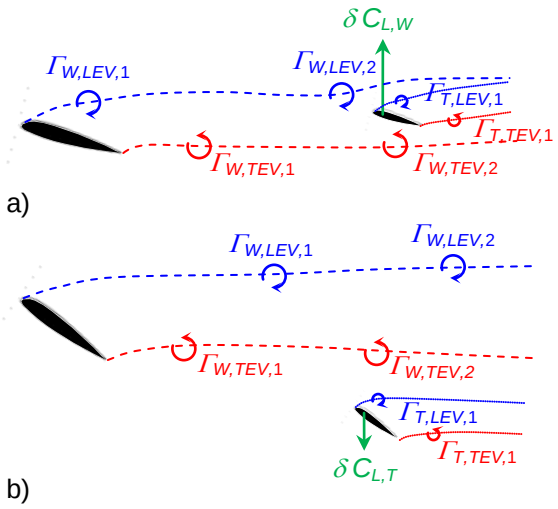

Figure 17. Pathlines of the LEV (blue) and TEV (red) of both airfoils for $\alpha = 30°$

The lift coefficient variation for the wing-tail configuration can be explained in comparison with a single airfoil case by a potential flow approach, for the angles-of-attack considered (Figure 17). For $\alpha = 15°$, the wing LEV are advected near the tail suction side, which, according to Kutta-Joukowski theorem, leads to an increase of the local circulation of the tail (Figure 17-a), and an increase of the averaged lift coefficient $\delta C_{L,W} > 0$. For $\alpha = 30°$, the wing TEV, in counter-rotation from the LEV, are advected near the tail suction side, and get a negative contribution to the tail circulation (Figure 17-b). As a consequence, there is a drop of the averaged lift coefficient $\delta C_{L,W} < 0$.

6. VORTEX SHEDDING FREQUENCY

The shedding period T can be measured for the wing airfoil, considering a Taylor hypothesis assuming the advection of vortices by the upstream flow velocity:

$$T = \frac{\delta x}{U_\infty} \tag{4}$$

with T the shedding period, U_∞ the upstream flow velocity and δx the spacing between two successive detached vortices. The corresponding shedding frequency and Strouhal number are built with:

$$St = \frac{f\,c}{U_\infty} = \frac{c}{T\,U_\infty} \tag{5}$$

with f the shedding frequency.

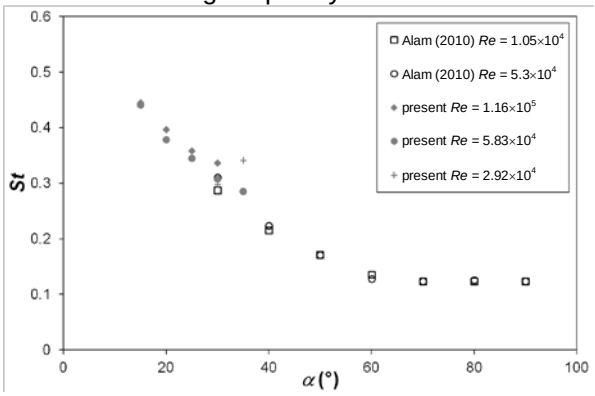

Figure 18. Vortex shedding Strouhal number versus angle-of-attack for a NACA 0012 airfoil [6] and a NACA 23 012 airfoil (present).

The development of Strouhal number versus angle-of-attack is plotted in Figure 18 and compared with measurements on a NACA 0012 airfoil [6]. A good arrangement of the measurement points is found, with a linear decrease of Strouhal number between $\alpha = 15°$ and 60° and a constant value of 0.12 for $\alpha > 60°$.

7. CONCLUSION

A reference 2D experiment of wing-tail configuration is implemented in a wind tunnel to get the PIV velocity field. The wing suction side detached flow for large values of the angle-of-

attack leads to the development of a Kelvin-Helmholtz like instability and the generation of LEV. As a consequence, the Kelvin theorem imposes the development of TEV, the periodic shedding of both vortical structures modifies the upstream flow conditions on the downstream tail airfoil. For α = 15°, the LEV pathlines are near the tail suction side, leading to a positive lift variation in comparison with the case of a single tail airfoil. For α = 30°, the TEV pathlines are near the tail suction side, leading to a negative lift variation in comparison with the case of a single tail airfoil. The lift coefficient changes for the interaction between two airfoils. This is not resulting from the tail airfoil placed in the wing recirculation, but from a vortex interaction with the tail. Depending on the sign of the circulation associated to the vortex passing in the tail airfoil suction side, we observe an increase or a decrease of the lift coefficient. The application of that result to flight dynamic model is that the deep stall phenomenon is generally attributed to a drop of dynamic pressure upstream of the tail. However, a drop of lift can be due to a velocity decrease but also a circulation decrease, which can be proved by the vortex-tail interaction. The perspective of the study is a characterization of the vortex-tail interaction for different wing-tail distances ℓ_x, ℓ_z. A potential model of the vortex-airfoil interaction will be built to understand the time-development of the lift modulation. The PIV and aerodynamic coefficients database will be used to validate a flight dynamic model.

8. REFERENCES

[1]. Mueller, T.J., DeLaurier, J.D. (2003). Aerodynamics of small vehicles, *Ann. Rev. Fluid Mech.* **35**, 89–111

[2]. Taylor, R.T., Ray, E.J. (1965) A systematic study of the factors contributing to post-stall longitudinal stability of T-tail transport aircraft, *AIAA Aircraft Design and Technology Meeting*, AIAA Paper 65-737, 12 p.

[3]. Bourgoyne, D.A., Ceccio, S.L., Dowling, D.R. (2005) Vortex shedding from a hydrofoil at high Reynolds number, *J. Fluid Mech.* **531**, 293-324

[4]. West, G.S., Apelt, C.J. (1982) The effects of tunnel blockage and aspect ratio on the mean flow past a circular cylinder with Reynolds numbers between 10^4 and 10^6, *J. Fluid Mech.* **114**, 361-377

[5]. Sheldahl, R.E., Klimas, P.C. (1981) Aerodynamic characteristics of seven symmetrical airfoil sections through 180-degree angle of attack for use in aerodynamic analysis of vertical axis wind turbines, *Sandia National Laboratories Report* SAND80-2114

[6]. Alam, M.M., Zhou, Y., Yang, H.X., Guo, H., Mi, J. (2010) The ultra-low Reynolds number airfoil wake, *Exp. Fluids*, **48**, 81-103

[7]. Hétru, L., Kolb, S., Montagnier, O., Faure, T.M. (2013) Tandem airfoil vortex interaction in deep-stall, *14th European Turbulence Conference,* paper ID 243, September 1-4, Lyon, France

[8]. Panah, A.E., Buchholz, J.H. (2014) Parameter dependence of vortex interactions on a two-dimensional plunging plate, *Exp. Fluids*, **55**,1687, 19 p.

[9]. Faure, T.M., Thach, H., Basley, J., Pastur, L., Lusseyran, F. (2010) Moyenne de phase spatiale appliquée à des champs PIV résolus en temps, *12ème Congrès Francophone de Techniques Laser*, Nancy (France), 14-17 Septembre, 111–118

[10]. Faure, T.M., Lusseyran, F., Pastur, L., Debesse, P. (2006) Développement d'instabilités dans un écoulement subsonique se développant au-dessus d'une cavité : mesures synchronisées PIV-LDV, *10ème Congrès Francophone de Techniques Laser*, Toulouse (France), 19-22 Septembre

[11]. Graftieaux, L., Michard, M., Grosjean, N. (2001) Combining PIV, POD and vortex identification algorithms for the study of unsteady turbulent swirling flows, *Meas. Sc. Technol.*, **8**, 1427-1440 (2001)